Neuron, Volume *89*

Supplemental Information

Grid Cell Responses in 1D Environments
Assessed as Slices through a 2D Lattice

KiJung Yoon, Sam Lewallen, Amina A. Kinkhabwala, David W. Tank, and Ila R. Fiete

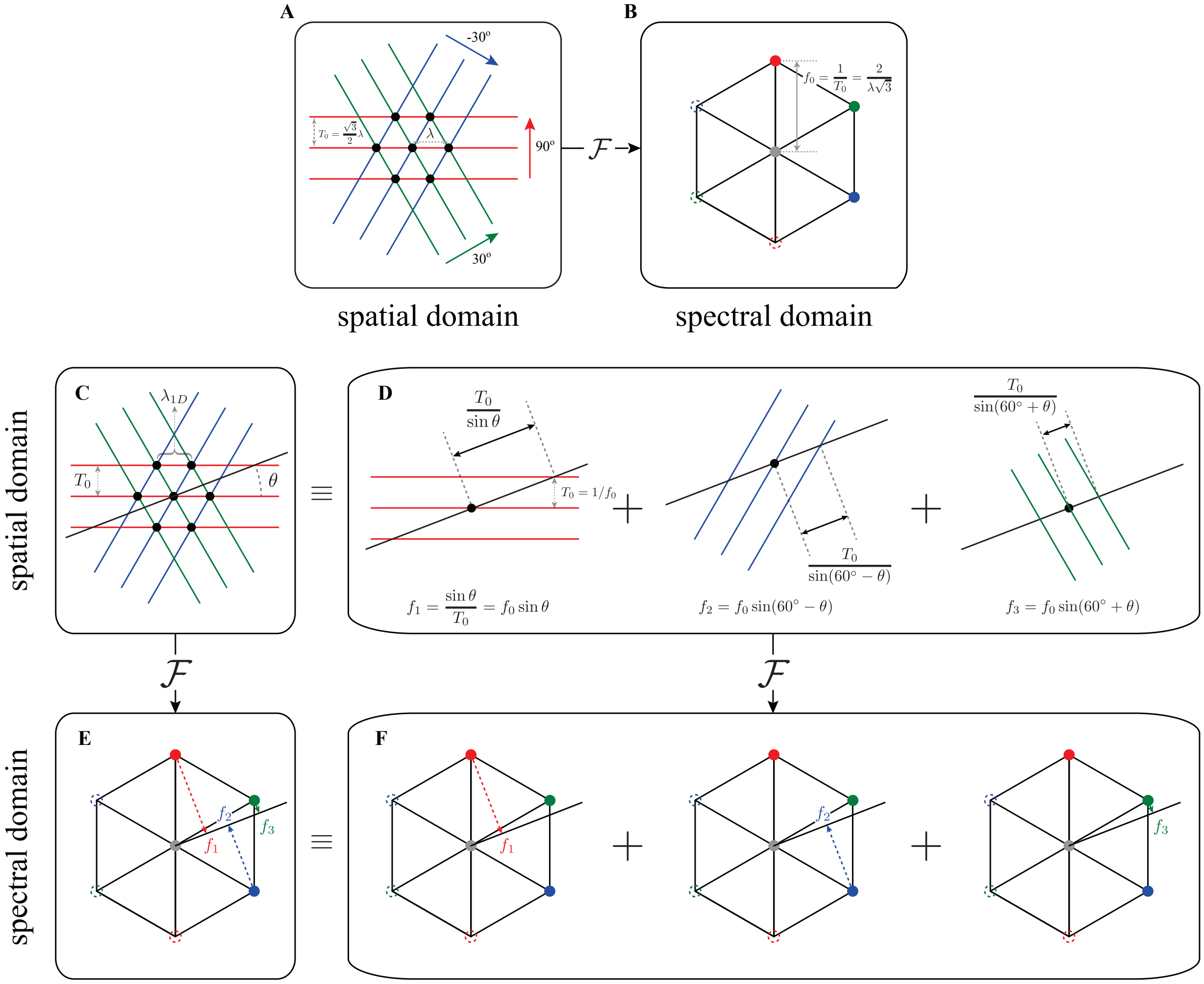

G

- $f_1 = \frac{2}{\sqrt{3}\lambda_{1D}} \sin\theta$
- $f_2 = \frac{2}{\sqrt{3}\lambda_{1D}} \left(\frac{\sqrt{3}}{2} \cos\theta - \frac{1}{2} \sin\theta \right)$

  $= \frac{1}{\lambda_{1D}} \left(\cos\theta - \frac{1}{\sqrt{3}} \sin\theta \right)$
- $f_3 = \frac{2}{\sqrt{3}\lambda_{1D}} \left(\frac{\sqrt{3}}{2} \cos\theta + \frac{1}{2} \sin\theta \right)$

  $= \frac{1}{\lambda_{1D}} \left(\cos\theta + \frac{1}{\sqrt{3}} \sin\theta \right)$

H

- $\lambda_{1D}^* = \frac{1}{\sqrt{f_1^2 + f_1 f_2 + f_2^2}}$
- $\theta^* = \sin^{-1} \left(\frac{\sqrt{3}\lambda_{1D}^*}{2} f_1 \right)$
- $\alpha^* = \frac{\lambda_{1D}^*}{\lambda_{2D}}$

Figure S1, related to Figures 1 and 2: **Duality of the spatial and Fourier spectral domain characterizations of a triangular lattice & its geometric interpretation.** (A) A triangular lattice consists of three sinusoidal plane waves related by 60° rotations. Here each line represents the crest of a wave (with period T_0). (B) Fourier transform of the triangular lattice: three positive and negative frequency vector pairs (positive = three colored dots; negative = dashed circles) that correspond to the frequency and directionality of the three plane waves in (A). (C) The triangular lattice of (A), together with a linear slice at angle θ (black line). (D) A linear slice through the full lattice equals the sum of a linear slice (at the same angle) through each plane wave. The individual slices result in periodic profiles with frequencies f_i, with $i \in \{1,2,3\}$, respectively. (E) Through the equivalence between (A) and (B), the frequency f_i can be derived by projecting the corresponding spectral peak (the corresponding colored dot) of i^{th} sinusoidal wave onto a line at the same angle, θ, though the figure in (B). (F) Because the Fourier transform is a linear operation, the combined projection in Fourier space of the sum of the 3 waves is the same as the sum of the three individual wave projections in Fourier space. (G) The locations in Fourier space of the three spectral peaks (f_i) depend on the period of the 2D lattice underlying the 1D response (λ_{1D}) and the slice angle (θ). (H) The analytical solution for slice parameters. Note that the equations in (G) correspond to an overdetermined system (three equations for the two unknowns, θ and λ); thus, the solutions in (H) are based on only the first two spectral peak frequencies. To find the best-fit linear slice, we consider all mappings of the significant spectral peaks in the data to the variables f_1, f_2 (see Experimental Procedures).

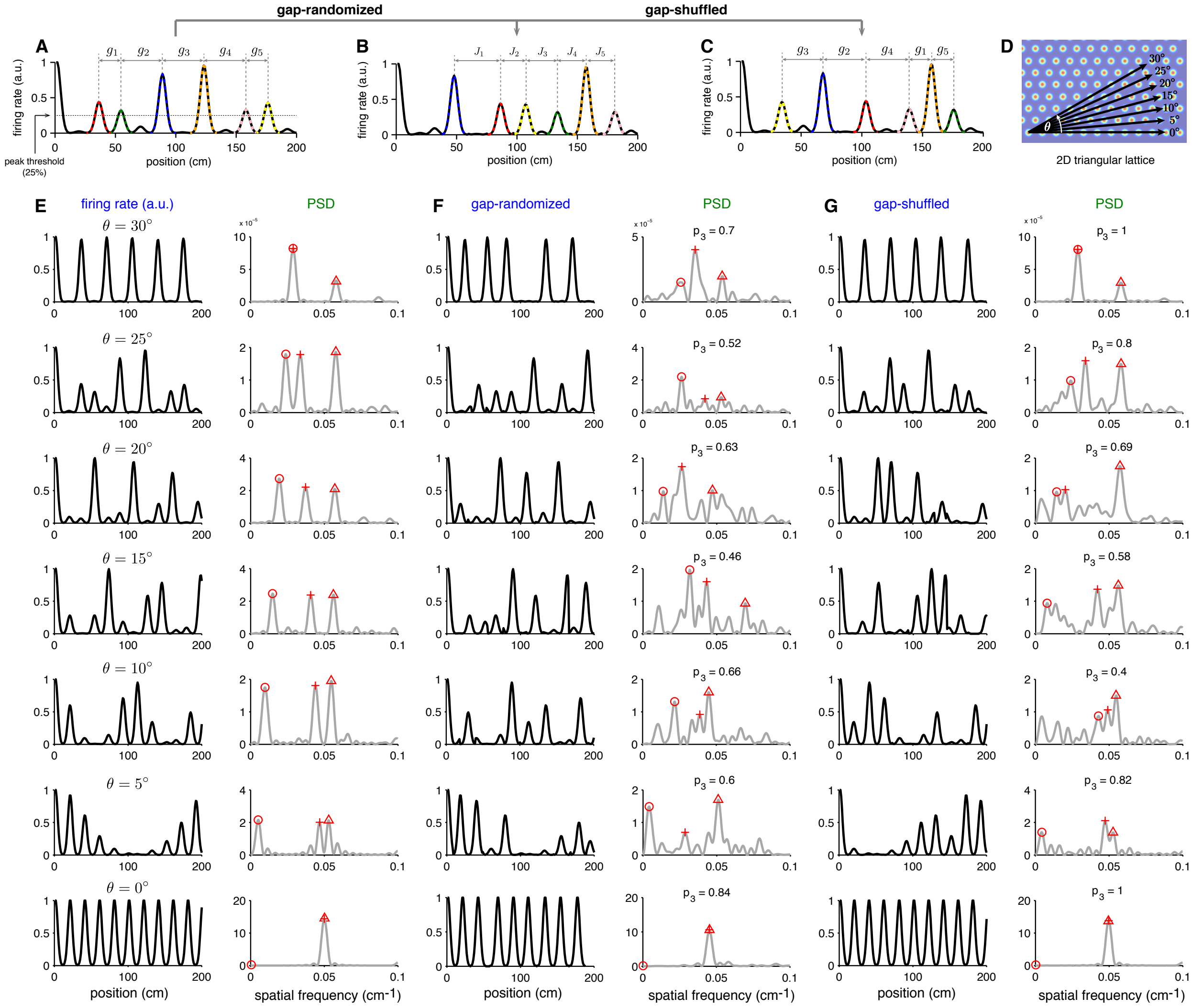

Figure S2, related to Figures 2 and 5, and Experimental Procedure: **Procedure for generating random control data & features of the PSD for random control data.** (A) An ideal linear slice (black) through a 2D lattice. Fields correspond to local maxima above a certain threshold (25% of the maximum firing rate); the start and endpoints of each field are defined to be the local minima on either side of the corresponding maximum. The g_i denote the gap lengths (distances between adjacent fields). (B) For the gap-randomized control, we choose a new center at random for each field, subject only to the condition that the new fields do not overlap. The background signal (black) is repartitioned according to the new field locations. The new gaps (J_i) will generally be highly uncorrelated with the original gaps (g_i). (C) Gap-shuffled controls are generated by shuffling the order of the gaps and the order of the firing fields. The gaps as a set are unchanged. (D-E) Same as Figures 2A-2C. (F) Gap-randomized controls for the perfect slices in column E (black, left) followed by their PSDs (gray, right). The three-peakiness score (p_3) is shown above each PSD. (G) Same as (F), for the gap-shuffled controls.

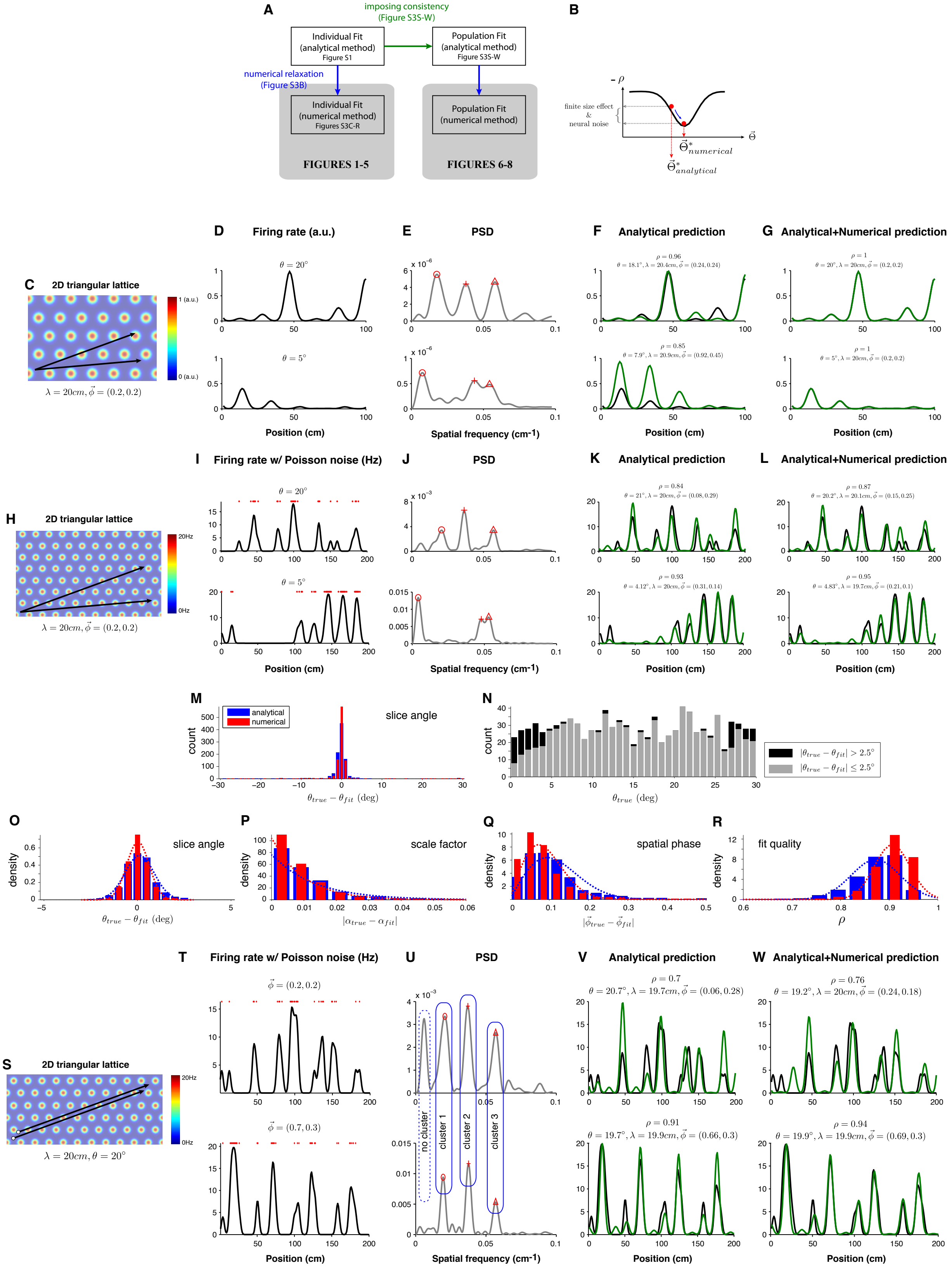
A
imposing consistency
(Figure S3S-W)
Individual Fit
(analytical method)
Figure S1
Population Fit
(analytical method)
Figure S3S-W
numerical relaxation
(Figure S3B)
Individual Fit
(numerical method)
Figures S3C-R
Population Fit
(numerical method)
FIGURES 1-5
FIGURES 6-8
B
$-\rho$
finite size effect
&
neural noise
$\vec{\Theta}$
$\vec{\Theta}^*_{numerical}$
$\vec{\Theta}^*_{analytical}$
C
2D triangular lattice
1 (a.u.)
0 (a.u.)
$\lambda = 20cm, \vec{\phi} = (0.2, 0.2)$
D
Firing rate (a.u.)
$\theta = 20°$
$\theta = 5°$
Position (cm)
E
PSD
x 10^-6
Spatial frequency (cm-1)
F
Analytical prediction
$\rho = 0.96$
$\theta = 18.1°, \lambda = 20.4cm, \vec{\phi} = (0.24, 0.24)$
$\rho = 0.85$
$\theta = 7.9°, \lambda = 20.9cm, \vec{\phi} = (0.92, 0.45)$
Position (cm)
G
Analytical+Numerical prediction
$\rho = 1$
$\theta = 20°, \lambda = 20cm, \vec{\phi} = (0.2, 0.2)$
$\rho = 1$
$\theta = 5°, \lambda = 20cm, \vec{\phi} = (0.2, 0.2)$
Position (cm)
H
2D triangular lattice
20Hz
0Hz
$\lambda = 20cm, \vec{\phi} = (0.2, 0.2)$
I
Firing rate w/ Poisson noise (Hz)
$\theta = 20°$
$\theta = 5°$
Position (cm)
J
PSD
x 10^-3
Spatial frequency (cm-1)
K
Analytical prediction
$\rho = 0.84$
$\theta = 21°, \lambda = 20cm, \vec{\phi} = (0.08, 0.29)$
$\rho = 0.93$
$\theta = 4.12°, \lambda = 20cm, \vec{\phi} = (0.31, 0.14)$
Position (cm)
L
Analytical+Numerical prediction
$\rho = 0.87$
$\theta = 20.2°, \lambda = 20.1cm, \vec{\phi} = (0.15, 0.25)$
$\rho = 0.95$
$\theta = 4.83°, \lambda = 19.7cm, \vec{\phi} = (0.21, 0.1)$
Position (cm)
M
analytical
numerical
slice angle
count
$\theta_{true} - \theta_{fit}$ (deg)
N
count
$|\theta_{true} - \theta_{fit}| > 2.5°$
$|\theta_{true} - \theta_{fit}| \leq 2.5°$
θ_{true} (deg)
O
slice angle
density
$\theta_{true} - \theta_{fit}$ (deg)
P
scale factor
density
$|\alpha_{true} - \alpha_{fit}|$
Q
spatial phase
density
$|\vec{\phi}_{true} - \vec{\phi}_{fit}|$
R
fit quality
density
ρ
S
2D triangular lattice
20Hz
0Hz
$\lambda = 20cm, \theta = 20°$
T
Firing rate w/ Poisson noise (Hz)
$\vec{\phi} = (0.2, 0.2)$
$\vec{\phi} = (0.7, 0.3)$
Position (cm)
U
PSD
x 10^-3
no cluster
cluster 1
cluster 2
cluster 3
Spatial frequency (cm-1)
V
Analytical prediction
$\rho = 0.7$
$\theta = 20.7°, \lambda = 19.7cm, \vec{\phi} = (0.06, 0.28)$
$\rho = 0.91$
$\theta = 19.7°, \lambda = 19.9cm, \vec{\phi} = (0.66, 0.3)$
Position (cm)
W
Analytical+Numerical prediction
$\rho = 0.76$
$\theta = 19.2°, \lambda = 20cm, \vec{\phi} = (0.24, 0.18)$
$\rho = 0.94$
$\theta = 19.9°, \lambda = 19.9cm, \vec{\phi} = (0.69, 0.3)$
Position (cm)

Figure S3, related to Experimental Procedure: **Analytical and numerical approaches for fitting a linear slice.** (A) The Fourier analytical method (Figure S1) is a simple and fast way of finding the best-fit linear slice of an individual cell. The fit-quality using the analytical method can be limited by finite size effects (C-G) and neural noise (H-L). Additional numerical optimization via a simple gradient descent rule (blue arrow in (B)) can improve the quality of fit. For multi-cell simultaneous slice fits, the dimensionality of the model can be reduced by requiring a *consistent* or common selection of significant PSD peaks across cells (S-W). The motivating assumption is that simultaneously recorded cells from the same module will share similar slice structures (green arrow). (B) A schematic for how the numerical method can improve the fit quality (ρ). Θ is the set of slice parameters. **Finite size effect on Fourier analytical method.** (C) The same set of linear slices as in Figure 2 but of half the length and with a non-zero spatial phase. Resulting 1D responses (D) and PSD (E), with significant PSD peaks indicated by red symbols. The peaks are less separated than in Figure 2C. (F) Analytical slice prediction from PSD (green), with 1D response (black) for comaprison; (G) Same as (F), but with further numerical optimization (see Experimental Procedures), which better matches the 1D response. **The effect of neural variability on Fourier analytical method.** (H-L) Same sequence of plots as in (C-G), to study the effects of noisy responses on analytical and numerical slice fits. (H) Same set of linear slices as in Figure 2 but with non-zero spatial phase. (I) Noisy versions of 1D responses (black) resulting from a slice, by generating an inhomogeneous Poisson spike train (red dots) from the underlying slice rates. Numerical optimization improves the prediction in terms of fit-quality (L) as well as estimated slice parameters (M-R). (M-R) $N = 1000$ noisy 1D responses are obtained from linear 2D lattice slices with uniformly sampled slice angles ($0^\circ \leq \theta_{true} \leq 30^\circ$) and spatial phases ($[0,w0] \leq \vec{\phi}_{true} \leq [1,1]$), as in (H-I). (M) Histogram of errors in estimating slice angle with the analytical method alone (blue) and after adding the numerical optimization step (red). (N) Which slice angles result in larger estimation errors? Black: larger errors ($> 2.5^\circ$), gray: smaller errors. Larger estimation errors occur for slices close to 0 and 30 degrees. (O-R) Normalized histograms of errors in slice angle (O), scale factor (P), spatial phase (Q), and quality of fit (R) through the analytical method alone and supplemented by numerical optimization, based on all samples that did not induce very large estimation errors on slice angle (gray bars in (N)). Numerical optimization by construction improves fit quality, but it also lowers the estimation error on all slice parameters (O: P= 2×10^{-15}, P: P= 6×10^{-7}, Q: P= 5×10^{-13}, two-sample F-test, R: P= 2×10^{-20}, two-sample t-test). **Dimensionality reduction in fitting comodular cells through common selection of spectral peaks.** (S) Parallel linear slices with different spatial phase. (T) Noisy 1D responses from these parallel linear slices, generated as in (H-I), and corresponding PSDs (U). Most high spectral peaks (red symbols) are common in both PSDs and are aligned, but the PSD from the first slice (top) has a high peak that is missing from the second (blue dashed vertical bar, labeled "no cluster"). This difference is due to the noisy responses. We impose consistency across comodular cells by identifying a common set of three highest spectral peak neighborhoods across cells from the PSD product of all comodular cells; for each cell, when then pick the highest PSD peak in the three neighborhoods (see Experimental Procedures). This produces roughly but not strictly parallel linear slices for all comodular cells (V: analytical prediction, W: with further numerical optimization).

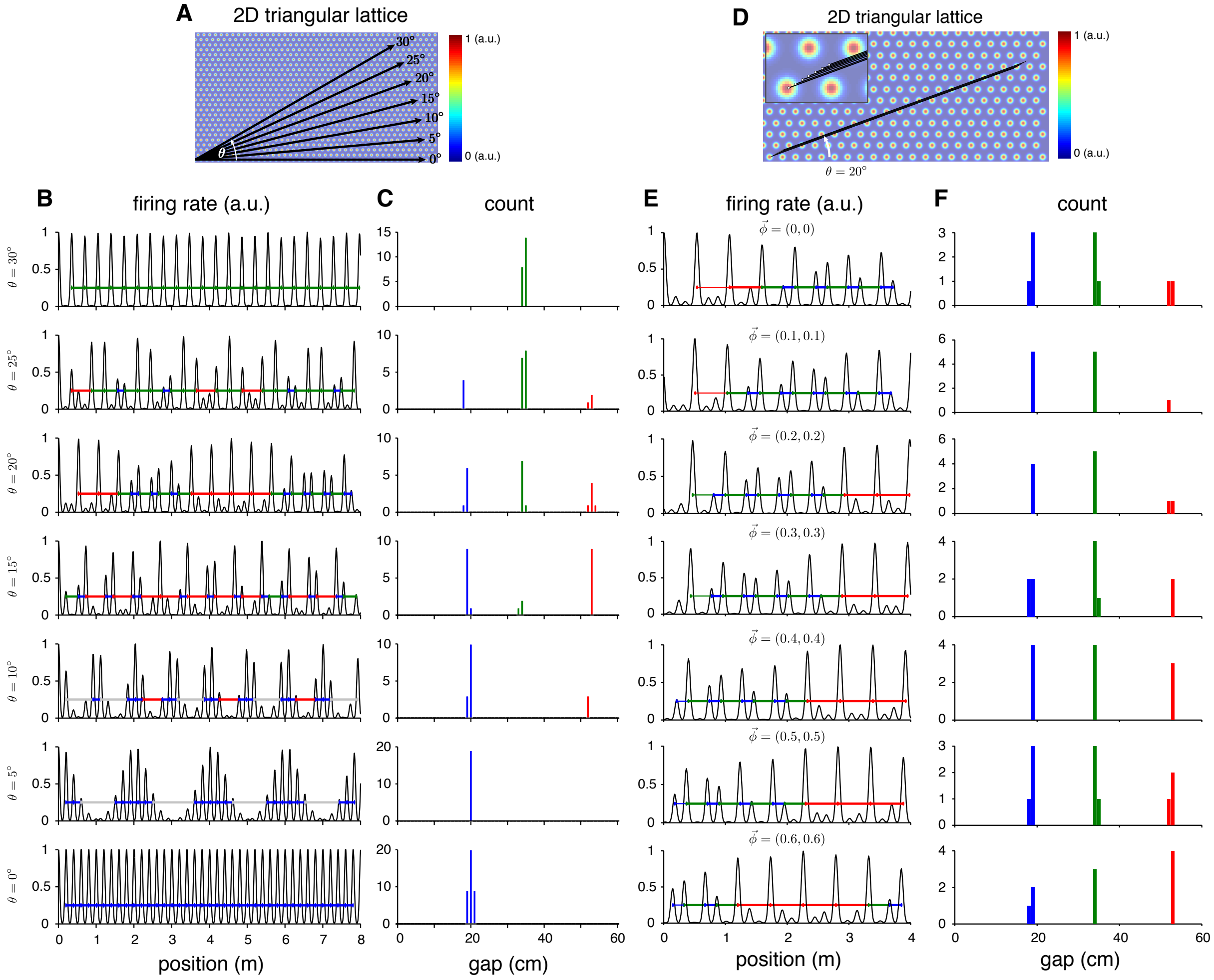
A
2D triangular lattice
30°
25°
20°
15°
10°
5°
0°
θ
1 (a.u.)
0 (a.u.)
D
2D triangular lattice
$\theta = 20^\circ$
1 (a.u.)
0 (a.u.)
B
firing rate (a.u.)
C
count
E
firing rate (a.u.)
F
count
$\theta = 30^\circ$
$\theta = 25^\circ$
$\theta = 20^\circ$
$\theta = 15^\circ$
$\theta = 10^\circ$
$\theta = 5^\circ$
$\theta = 0^\circ$
$\vec{\phi} = (0, 0)$
$\vec{\phi} = (0.1, 0.1)$
$\vec{\phi} = (0.2, 0.2)$
$\vec{\phi} = (0.3, 0.3)$
$\vec{\phi} = (0.4, 0.4)$
$\vec{\phi} = (0.5, 0.5)$
$\vec{\phi} = (0.6, 0.6)$
0 1 2 3 4 5 6 7 8
position (m)
0 20 40 60
gap (cm)
0 1 2 3 4
position (m)
0 20 40 60
gap (cm)

Figure S4, related to Figure 3: **Features of the gap distribution for linear slices of different angles and lengths & for parallel linear slices.** (A-C) Slices at different angles: different gaps are represented with different frequencies as the slice angle varies, but all the gaps at all angles belong to the same small set. (A) Slices at different angles through a 2D triangular lattice with a period of 20 cm. The slices are 4 times longer than those in Figure 2A. (B) 1D responses resulting from the linear slices in (A). Colored horizontal lines: gaps between significant fields, color-coded by length (blue: 20 cm, green: $20\sqrt{3}$ cm, red: $20\sqrt{7}$ cm, and gray: the rest. As before, significant fields are those whose maximum height exceeds 25% of the overall maximum. (C) Histogram of the gaps from (B), with the same color code. Up to small deviations, the gap histograms exhibit the same set of peaks across slice angles, but the height of each peak in the histogram varies with slice angle (with some peaks disappearing completely for certain slice angles). In addition, even for a fixed slice angle, the relative heights of the peaks in the gap distribution can vary with the length of the sampled 1D response, if it is sufficiently short. (It is easy to check directly that different subsamples of the full responses in (B) can yield distinct subcollections of gaps). (D) Parallel slices through a 2D triangular lattice with different spatial phases, as in Figure 2D. Inset: magnified view of the starting points (spatial phases) of the parallel linear slices. (E) 1D responses resulting from the linear slices in (D). (F) Histogram of the gaps from 1D responses in (E). As in (C), the gaps cluster around the same locations, despite having different spatial phases.

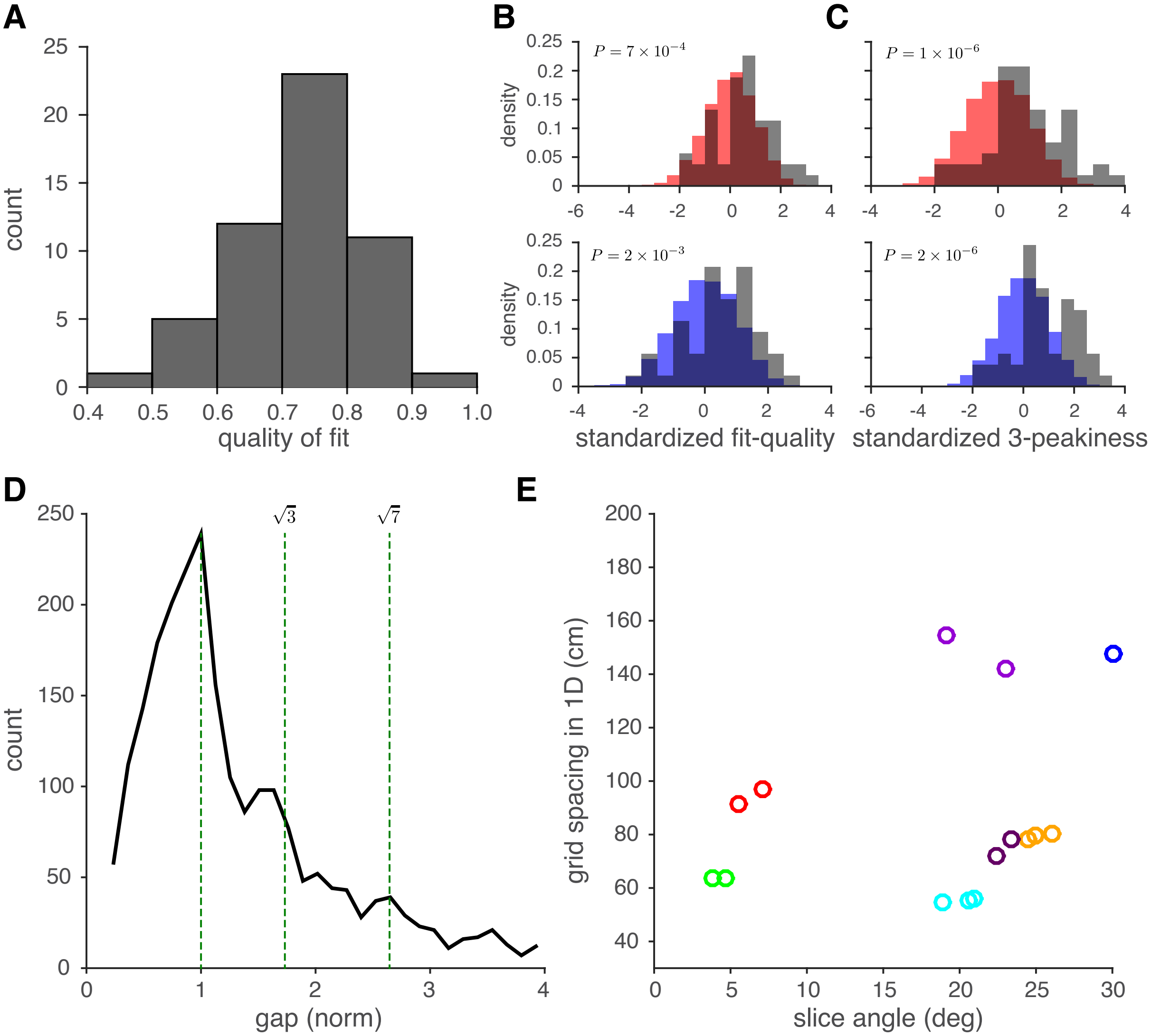

Figure S5, related to Figures 4, 5, and 6: **Analysis of 1D real linear track data.** This analysis involves all putative grid cells in the dataset from (Brun et al., 2008) (see Experimental Procedures for selection criteria). (A) Histogram of fit-quality of (the analytically predicted) linear lattice slice to the recorded 1D response. (B-C) Same as in Figures 5B-C: comparison of data slice fits with slice fits to gap-randomized and gap-shuffled controls . *p*-values noted in each figure, one-sample *t*-test. (D) Aggregate gap distribution (black) pooled across all cells in the dataset, after the gaps in each cell's response are normalized by the inferred 1D lattice period from the slice fit. (E) The inferred best-fit slice parameters for all cells, obtained individually per cell (no imposed consistency). Cells plotted in a common color: putative or inferred co-modular cells, classified as such if they are simultaneously recorded in the same animal and if their inferred periods are within 10% of each other. Note that there are two overlapping circles in dark blue at slice angle ≈ 30°.

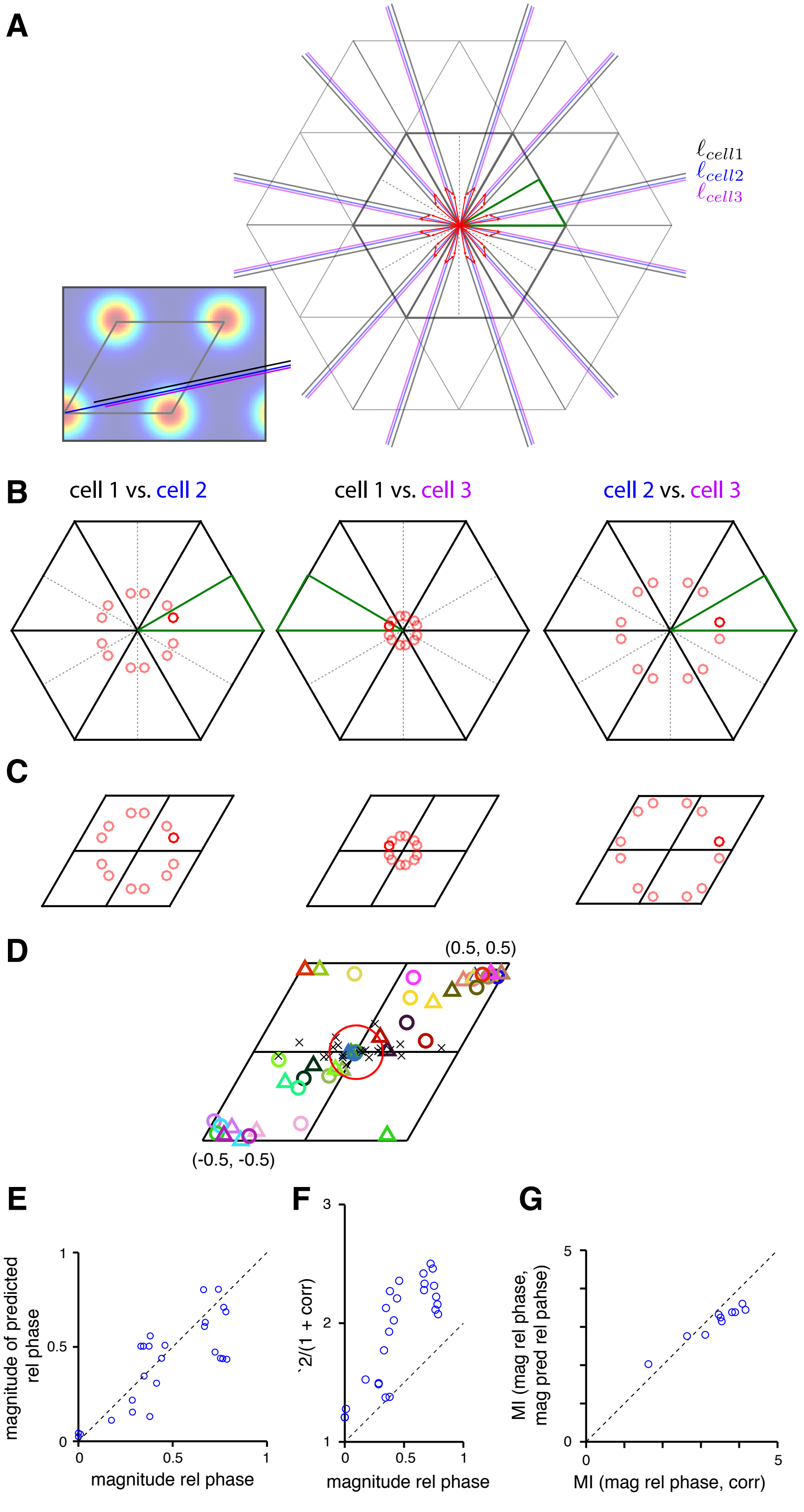
A
ℓ_{cell1}
ℓ_{cell2}
ℓ_{cell3}
B
cell 1 vs. cell 2
cell 1 vs. cell 3
cell 2 vs. cell 3
C
D
(0.5, 0.5)
(-0.5, -0.5)
E
magnitude of predicted rel phase
magnitude rel phase
0
0.5
1
F
`2/(1 + corr)
magnitude rel phase
1
2
3
G
MI (mag rel phase, mag pred rel pahse)
MI (mag rel phase, corr)
0
5

Figure S6, related to Figure 7 and Experimental Procedure: **Multiplicity of linear slices and ambiguity of the predicted 1D relative phase.** (A) Three parallel linear slices through a 2D lattice, with slice angles between 0° and 30° and spatial phases within a rhomboidal unit cell, generate a unique 1D response. The same response, however, can be generated by reflecting the linear slices over the line of 30° and/or by rotating the linear slices through multiples of 60° around the origin (black/blue/purple: a triple of parallel linear slices populated up to 12 identical pairs). The spatial phases resulting from these operations can be entirely different (red arrows, right), leading to an ambiguity in inferring the 2D spatial phase from the 1D response. (B) The 12 red circles from each column represent a clearer depiction of the equivalent relative phases from (A), separately for each cell pair. (C) The same as (B), but with all equivalent relative phases depicted within the same rhomboid unit cell. (D) The same as in Figure 7A except that the best relative phase estimates for pairs in each comodular $K-$tuple in the dataset are not generated pairwise but by selecting a single consistent solution out of the 12-fold degenerate domains for all (K choose 2) cell pairs at once. **Predictability of relative phase magnitude.** (E) Measured 2D relative phase magnitudes (abscissa) versus the magnitude of predicted values from slice analysis (ordinate). (F) Measured 2D relative phase magnitudes versus rescaled correlation coefficients between cell pairs' 1D responses. (G) Same as in Figure 7C, but based on data in (A-B). The magnitude of relative phase can be equally predicted by the slice analysis and correlation measure between cell pairs.

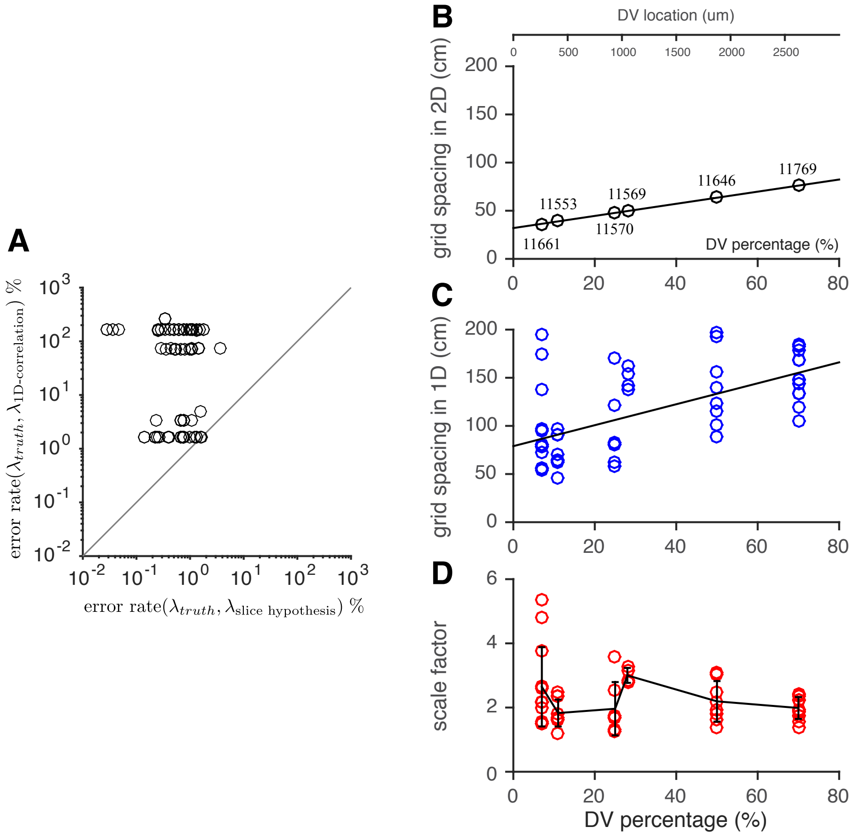

Figure S7, related to Figure 6: **Grid expansion from 2D to 1D real environments.** (A) A comparison of the information inferred about the underlying grid period of an ideal slice, via two different methods: the full slice-hypothesis based method presented in this paper (abscissa), and a method based on 1D correlation (ordinates). The black circles correspond to 100 slices with randomly chosen slice angles and spatial phase, ($\lambda_{\text{truth}} = 60cm$, and slice length $= 6m$. (B) Black line: Linear fit and extrapolation of the relationship between a cell's observed dorsoventral (DV) location and 2D grid period, based on Figure 2h in (Hafting et al., 2005). Circles: cells from (Brun et al., 2008), placed on the black line according to their observed DV locations (abscissa; data from Figure 1 in (Brun et al., 2008), coordinates obtained by orthogonal projection onto a DV axis). The ordinates obtained from the placement of these points correspond to the inferred 2D periods of these cells. (C) Blue circles: inferred 2D grid periods for the 1D responses from (Brun et al., 2008), using the slice-fit method of the paper (blue circles). Black: linear fit. (D) Red circles: Scale factor (red circles) obtained by taking the ratio of data in (C) to that in (B), for each cell.

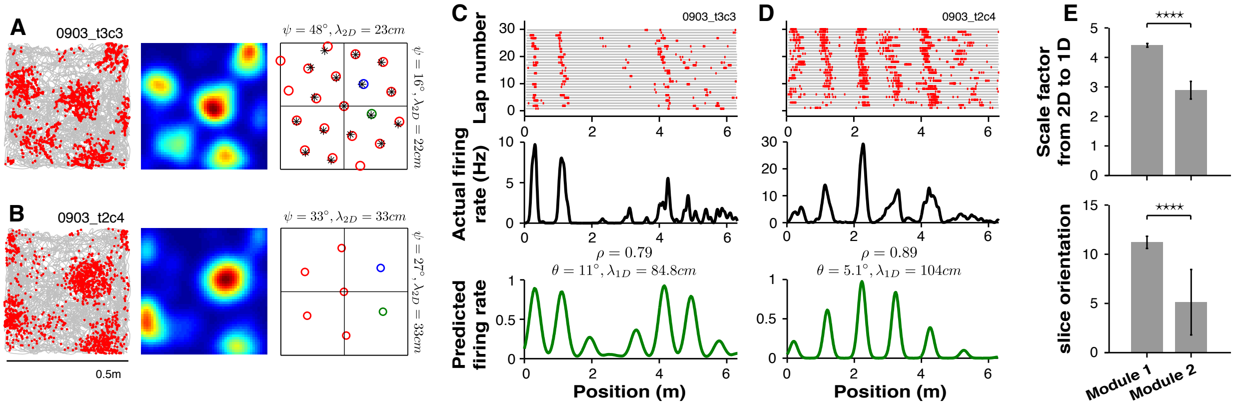

Figure S8, related to Figure 6: **Functional independence of grid modules.** (A-B) Two grid cells recorded simultaneously from different tetrodes in 2D open field. Left: Spike discharge map. Middle: Smoothed rate map. Right: Best-fit template lattice (red circles) to the autocorrelogram (top) and to the rate map (bottom). When the grid period is large and firing fields are mostly cropped, we searched for the best-fit template lattice directly in the rate map, which is the case for the bottom cell. Blue circle: End point of the first primary lattice vector (length and angle of the vector are shown on the top). Green circle: End point of the second lattice vector (length and angle are shown at the right). (C-D) Top: spike rasters of the same cells. Middle: Smoothed trial-average firing rate. Bottom: Rate prediction from a linear slice. (E) Both scale factor (top) and slice angle (bottom) do not change coherently during a complete environmental transition from 2D to 1D, when a cell pair is from different modules.

Supplemental Experimental Procedures

Binning and rate maps.

Cell-sorted spikes from foraging mice were assigned to 1 cm × 1 cm spatial bins (2D open field) or 1 cm spatial bins (1D linear track). Positions were derived from samples taken at 30 Hz. The number of spikes assigned to a bin was divided by the rat's total dwell time in that bin, to remove the effects of inhomogeneous spatial exploration on estimating the probability of spiking at each location. This defined the rate map. Smoothed rate maps were generated by convolving the binned rate maps with a 2D or 1D Gaussian kernel, respectively ($\sigma = 4$ bins).

Cell selection.

We analyzed units from (Domnisoru et al., 2013), which were recorded in both 2D open fields and on virtual 1D linear tracks. Our starting sample consisted of 126 units (137 recorded, with 126 of these passing an interspike interval criterion that no more than 0.25% of spikes in each unit were emitted with interspike intervals (ISIs) shorter than 1 ms (Domnisoru et al., 2013)).

We applied the intersection of three criteria on spatial tuning to select units individually, then excluded duplicate units by a separate criterion based on similarity of tuning. These methods are described below. The result was 25 grid units (6 singles, 3 pairs, 2 quadruples, and 1 quintuple) from the starting sample of 126.

Our selection procedure follows: We first computed three scores that reflect spatial response properties individually for each unit: 1) A standard gridness score (Langston et al., 2010) on the 2D spatial tuning, to determine whether the unit has sufficiently grid cell-like tuning. 2) A score on the overall stability of the response in 1D (see Trial selection, below) computed on the most-stable 30-trial block out of the variable number of trials recorded for each unit, to remove units that do not display a stable spatial response in 1D because we could not average trials to obtain a 1D spatial tuning curve. 3) The entropy of the 1D spatial tuning curves (with the spatial tuning curve obtained from averaging the most-stable 30 trials for each cell). High entropy units have high background firing, little spatial modulation, large drifts, or generally high noise in their responses. This entropy score also helps to catch units with variable or drifting trial-to-trial responses that are not caught by the stability measure in (2) above.

Units with 2D gridness < 0.34 (Domnisoru et al., 2013), 1D stability < 0.1, and 1D entropy > 8.7 were rejected, reducing the sample size from 126 to 26 units (Individually, 69 units fail the 2D gridness score, 39 fail the stability score and 64 fail the entropy score). Units had two kinds of stability problems in 1D: one was a slow, systematic drift of firing field locations across trials; the other was strongly fluctuating spike counts and other less-systematic effects from trial to trial. Both led to less-sharp 1D tuning curves with lower signal-to-noise ratio. The stability and entropy thresholds quoted here were set to eliminate excess drift and variability based on empirical observation of the 1D track spike rasters.

Finally, to avoid overcounting one cell as two units, we eliminated one unit out of each simultaneously recorded pair if they exhibited both very similar spatial tuning and a large amount of mutual spike contamination (Cell pairs with very similar tuning but small or no spike contamination are legitimate independent samples and should both be included – grid cells within a population are expected to have a spectrum of relative phases, including a relative phase of zero). For a cell pair with relative phase magnitude smaller than 10% of the maximal possible relative phase separation, and a contamination score (defined below) greater than 0.1, we kept only one cell of the pair (the one with the higher gridness). This process identified a single pair of units from the set of 26 (suggesting one double-counted cell), and led to the final dataset of 25 units.

Entropy.

Entropy is given by the standard definition:

$$\text{Entropy} = -\sum_i P(x_i) \log P(x_i)$$

where $P(x_i)$ is the firing rate in the ith spatial bin along the linear track, normalized by the area of the full firing rate curve (firing rate per bin, summed over all bins).

Comodularity.

Cells were defined as comodular if they were recorded simultaneously from the same animal and if the spatial periods of their recorded 2D responses differed by less than 10% (relative to the larger of the two estimated periods) and the 2D grid orientations differed by less than 10 degrees.

Spike cross-contamination for cell pairs.

Following (Hill et al., 2011), we fit the pair of clusters C_i and C_j comprised of the waveforms of all spikes from two simultaneously recorded units i, j by a sum of (two) Gaussians. With this fit, we derive a contamination score as the average probability that a spike from C_i would come from C_j's distribution:

$$\text{contamination}(C_1, C_2) := \frac{1}{N_1} \sum_{v \in C_1} P(C = C_2 \mid V = v)$$

Additional cells from real 1D tracks.

We additionally studied the 1d real-track responses of cells from (Brun et al., 2008). As stated in the main manuscript, for left-to right traversals we used only the left (first) half of the track, and for right-to-left traversals, we used the right (first) half of the track. When we refer to track length L in the analysis below, we refer to these first half-tracks. The responses of a cell on the two different direction traversals were treated as two independent spatial responses. We possess no ground-truth data on which responses in (Brun et al., 2008) come from grid cells. Thus, we must identify responses as coming from putative grid cells based on characteristics of the spatial response. We do so as follows:

The selection criteria for identifying putative grid cells from (Brun et al., 2008) are adapted from Domnisoru et al. 2013, with adjustments to simplify the criteria slightly and take into account the very different track length. The modified criteria are as follows: A 1D response cannot be a putative grid cell response if (a) the number of transitions N_{trans} between an in-field and and out-of-field period for a track of length L is smaller than $L/(5\langle w \rangle)$, where $\langle w \rangle$ is the mean firing field width for that 1D response. (In-field and out-of-field periods are defined below.) (b) The widest field of the response has width greater than $5\langle w \rangle$. (c) Same as in (Domnisoru et al., 2013), which is that 30% or fewer of the bins are assigned to either in-field or out-of-field periods. (d) the mean firing rate in-field divided by the mean firing rate out-of-field is smaller than 2.

The definitions of in-field and out-of-field periods are very similar to (Domnisoru et al., 2013), but the numerical thresholds are changed and some of the steps are simplified: out-of-field periods are defined as intervals of $\geq 8cm$ for which the firing rate was lower than the 20th percentile of the bootstrapped shuffle distribution for that bin (i.e., $1 - P_{value} \leq 0.2$). Firing fields are intervals of duration $\geq 12cm$ with firing rate higher than the 80th percentile of the bootstrapped shuffle distribution for that bin (i.e., $1 - P_{value} \geq 0.8$). There is no change in criteria for defining firing fields if they occurred at the ends of the track. Bins with intermediate firing rates remained unassigned. Steps omitted from (Domnisoru et al., 2013) criteria for simplicity: we did not extend candidate firing fields by an adjacent bin on each side if their firing rates exceeded the 70th percentile of the bootstrapped shuffle distribution for that bin; we did not examine and discard fields based on whether they received spike contributions from only $\leq 20\%$ of all trials.

If the response of a cell in either traversal direction survived the selection process above, the cell was classified as a putative grid cell. We were left with 51 putative grid cells with 65 passing spatial responses, out of the full dataset of 97 total cells with 194 spatial responses. We applied slice fits to all 65 passing responses, provided they had ≥ 3 fields on the length-L half-track (this condition is necessary for generating meaningful slice fits: two 1D fields are mathematically not enough of a constraint to specify a slice or infer the underlying grid cell period, by any method). This leaves 40 putative grid cells and 53 responses; the excluded cells here tend to be from the most ventral end of the dorsolateral MEC.

Trial selection.

Different cells were recorded for different numbers of trials, and some cells showed substantial drift in their spatial tuning across trials. To equalize the number of trials used per cell and obtain the most stable block of trials for each cell so that we could obtain reasonable trial-averaged rates, we adopted the following trial-selection procedure for Figures 1-8: Given a total of $N > 30$ trials, we computed a stability score, defined as the average of the pairwise Pearson's correlation coefficient across all pairs of single-trial rate responses (obtained by smoothing the single-trial spiking responses, as described in *Binning and rate maps* above) within the consecutive 30-trial block $[i, i+29]$. We repeated this process for different starting positions i in steps of 1 trial, starting from $i = 1$ up to $i = N - 29$. From this analysis, we selected the 30-trial block with the largest stability score; for comodular cells, we selected a common 30-trial block with the largest stability score averaged across cells.

Fourier spectral analysis for inferring 2D lattice slice parameters from a 1D response: theory.

Consider a 2D firing rate $r(\mathbf{x})$, $\mathbf{x} = (x_1, x_2)$, consisting of identical 2D bumps centered at the vertices of a triangular lattice with period λ. For example, with Gaussian bumps of unit height and variance σ^2, r is given by the formula

$$r(\mathbf{x}) = \sum_{\mathbf{v}\in\Gamma} e^{-\|\mathbf{x}-\mathbf{v}\|^2/2\sigma^2},$$

where $\Gamma = \{m\lambda(1,0) + n\lambda(1/2, \sqrt{3}/2)\}$ for all integers m and n. The details of the bump shapes are inessential for the following derivation, as long as they are sufficiently narrow relative to the lattice spacing λ.

In this case, the power spectrum of r will be dominated by equal contributions from three frequencies $\{\mathbf{b}_1, \mathbf{b}_2, \mathbf{b}_3\}$, where $\mathbf{b}_1 = \frac{1}{\lambda}(0, 2/\sqrt{3}), \mathbf{b}_2 = \frac{1}{\lambda}(1, -1/\sqrt{3}), \mathbf{b}_3 = \frac{1}{\lambda}(1, 1/\sqrt{3})$ (Figure S1). Therefore the response can be approximated as the sum of three 2D sine waves along these directions:

$$r(\mathbf{x}) \approx \sum_{i=1}^{3} \rho \cos\left(2\pi \mathbf{b}_i \mathbf{x}^T\right) \tag{1}$$

where the superscript T on a vector refers to the vector transpose, $\mathbf{x}\mathbf{y}^T$ is the dot product between vectors $\mathbf{x}, \mathbf{y}$, and ρ is the relevant Fourier coefficient. For simplicity, we scale $r(\mathbf{x})$ to make $\rho = 1$ in what follows.

Now consider the line $\mathbf{x}_\ell(t)$ parametrized by t in the 2D coordinate space above, with origin at $\mathbf{c} = \lambda(\phi_1, \phi_2)$ and angle θ relative to the x-axis. It is given by

$$\begin{aligned} \mathbf{x}_\ell(t) &= (\cos(\theta), \sin(\theta))\,t + \mathbf{c} \qquad (2) \\ &\equiv \mathbf{u}(\theta)\,t + \mathbf{c} \qquad (3) \end{aligned}$$

where we have defined the vector $\mathbf{u}(\theta) = (\cos(\theta), \sin(\theta))$.

The modulation of firing rate r along this line is given by restricting $r(\mathbf{x})$ to the coordinates $\mathbf{x}_\ell(t)$. Thus, along the line, the rate varies as:

$$r(\mathbf{x}_\ell(t)) = \sum_{i=1}^{3} \cos\left(2\pi\,\mathbf{b}_i\,\mathbf{x}_\ell(t)^T\right) \tag{4}$$

$$= \sum_{i=1}^{3} \cos\left(2\pi\,\mathbf{b}_i\,\mathbf{u}(\theta)^T t + 2\pi\,\mathbf{b}_i\,\mathbf{c}^T\right) \tag{5}$$

$$= \sum_{i=1}^{3} \cos\left(2\pi f_i(\lambda,\theta)t + 2\pi\delta_i(\mathbf{c})\right) \tag{6}$$

where $f_i(\lambda,\theta) \equiv \mathbf{b}_i(\lambda)\,\mathbf{u}(\theta)^T$ and $\delta_i(\mathbf{c}) \equiv \mathbf{b}_i(\lambda)\,\mathbf{c}^T$ are all scalar quantities (we have made the dependence of the $\mathbf{b}_i$'s on λ explicit here because λ is a slice parameter we would like to infer from the following analysis, as is θ).

From Equation 6, it is clear that the Fourier transform of $r(\mathbf{x}_\ell(t))$ will have spectral peaks at the frequencies $f_1(\lambda,\theta)$, $f_2(\lambda,\theta)$, $f_3(\lambda,\theta)$ and phases $2\pi\delta_1(\mathbf{c}), 2\pi\delta_2(\mathbf{c}), 2\pi\delta_3(\mathbf{c})$ (Figures S1C-F).

Given the Fourier transform of $r(\mathbf{x}_\ell(t))$ (more specifically, given the six scalars $\{f_i | i = 1,2,3\}$ and $\{\delta_i | i = 1,2,3\}$), our goal is to extract four quantities: the period and angle parameters (λ,θ) of the slice as well as the vector origin of the slice, recast as a phase with respect to a unit vector of the lattice, given by the vector $\phi \equiv \mathbf{c}/\lambda$.

For any equilateral triangular lattice (characterized by the three vectors $\mathbf{b}_1, \mathbf{b}_2, \mathbf{b}_3$ specified above) it is easy to see that $\mathbf{b}_1 + \mathbf{b}_2 - \mathbf{b}_3 = 0$. As a result, $f_1 + f_2 - f_3 = (\mathbf{b}_1 + \mathbf{b}_2 - \mathbf{b}_3)\,\mathbf{u}(\theta)^T = 0$ (Figure S1G). Thus, only two of the f_i's provide independent information and a pair of f_i's is sufficient to analytically obtain λ, θ. The corresponding two δ_i's are sufficient to analytically determine the slice origin vector $\mathbf{c}$. This procedure will produce a reasonable solution if a recorded rate is indeed a slice.

Note that the scale factor (α) referred to in the main manuscript is defined as λ (the inferred period of the lattice that underlies the 1D response), divided by the measured period of the cell's response in 2D (λ_{2D}). Thus, $\alpha = \lambda/\lambda_{2D}$. The inferred 2D phase from the 1D slice analysis in the main manuscript is $\phi = \mathbf{c}/\lambda$; we write it in terms of the oblique projection onto the two primary lattice vectors (Yoon et al., 2013).

Direct inference of 2D relative phase from a pair of 1D responses.

The relative 2D phase between two linear slices is simply the difference in the estimates of the 2D phases of each of the two slices ($\Delta\phi \equiv \phi^1 - \phi^2$, where ϕ^1, ϕ^2 are the 2D phases of each linear slice).

However, it is also possible to directly infer the relative 2D phase from the two 1D responses, using the cross-correlation theorem:

$$\mathscr{F}\left[(g \star h)(t)\right] \quad = \quad G(f)\overline{H(f)} \tag{7}$$

where $\star$ denotes the correlation and G, H are the Fourier transforms of g, h, respectively. The Fourier transform of the cross-correlation of the two signals g, h (the left hand side of Equation 7) will have phase $2\pi\delta_i(\mathbf{c}_g - \mathbf{c}_h)$ (as in Equation 6) ascribed to the conjugated $H(f)$, which can be directly recast as a 2D relative phase, $\Delta\phi = (\mathbf{c}_g - \mathbf{c}_h)/\lambda$.

Fourier spectral analysis for inferring 2D lattice slice parameters from a 1D response: practice.

For each cell recorded in 1D (or each random control response), we first compute the PSD of its response, identify the two highest peaks in its PSD, and label the peak locations (i.e. the spatial frequencies at which the peaks occur) as q_1 and q_2 with $q_1 < q_2$. Given (q_1, q_2), there is a choice in whether (q_1, q_2) should be identified with (f_1, f_2), or (f_1, f_3), or (f_2, f_3) in the analytical definitions above. We consider the three possible solutions, in addition to the two solutions corresponding to the special cases of a 0 or 30 degree slice (for which there are only two spectral peaks, see Figure 2). From this set of 5 discrete slice solutions, we pick the one with the best correlation with the recorded 1D response of the cell. The 2D period, obtained from 2D recordings for each cell, was set to the average of lengths of two primary lattice vectors.

Note that different assignments of the two highest peaks to the f_i's (three of the five candidate solutions described above) can correspond to different local minima in the solution space; sometimes, these different local minima can provide roughly similar (in terms of correlation coefficient) slice fits to the measured 1D response. We explore this issue further in Figure 6 of the main manuscript.

We numerically refined the analytical solution by searching locally for values of the four slice parameters (θ, α, ϕ) that optimized the fit between the recorded 1D rate response and rate values predicted by the slice. The fit is quantified by Pearson's correlation coefficient (ρ). The slice parameters were initiated to the analytical solution $(\theta^*, \alpha^*, \vec{\phi}^*)$

then locally relaxed via a standard gradient ascent algorithm under the following constraints: $\max(0^\circ, \theta^* - 3^\circ) \leq \theta \leq \min(30^\circ, \theta^* + 3^\circ)$, $\alpha^* - 0.5 \leq \alpha \leq \alpha^* + 0.5$, and $[0,0] \leq \vec{\phi} \leq [1,1]$.

Generating matched random control data.

Consider a cell with spatial tuning curve $\mathbf{r}(x)$, measured over the range $x \in [0, x_{max}]$. We generate two kinds of matched controls for this cell: gap-randomized and gap-shuffled. For both types of control, we first process the data as follows.

For each spatial tuning curve, identify the locations of all peaks and troughs. Significant peaks are those whose heights exceed 25% of the maximal firing rate in the tuning curve. Label the locations of these peaks $\{p_i\}$ (with $i = 1, \cdots, Q$ and $p_1 < \cdots < p_Q$). We seek to identify firing fields, which may include more than one significant peak if the peaks are very closely spaced. Label a set of consecutive significant peaks as belonging to the same field if they are closer to each other than half the estimated field width for the cell (field width w is defined as the distance from the origin to the first trough in the autocorrelogram of $\mathbf{r}(x)$). In other words, K consecutive peaks indexed $i, i+1, \cdots, i+K-1$ belong to a single field if $p_{j+1} - p_j \leq w/2$ for each $j = i, \cdots, i+K-2$. (For a well-isolated peak separated by $> w/2$ from the rest, $K = 1$.) We now define a field interval as the spatial interval encompassing these K peaks, with the interval boundaries given by the closest troughs immediately flanking to the left and to the right the set of K peaks. Starting from the first significant peak in the spatial response, we identify field intervals as described above, and denote the αth field interval as $[x_s^\alpha, x_e^\alpha]$, where x_s^α, x_e^α are the start and end coordinates marked by the two troughs surrounding the field. The intervals $[x_e^\alpha, x_s^{\alpha+1}]$ between field intervals (and also the interval $[0, x_s^1]$), if non-empty, are designated non-field intervals.

Suppose the cumulative length of all L field intervals put together covers M bins, while the cumulative length of the full track covers $N = x_{max}/\Delta x$ bins, where Δx is the width of each spatial bin ($\Delta x = 1$cm; x_{max} and Δx have dimensions of centimeters, while L, M, and N are dimensionless). Then the cumulative length of non-field intervals covers $N - M$ bins.

To generate gap-randomized controls, we take the following steps: first generate a set of $N-M+L$ empty slots. Randomly and without replacement, assign each of the indices $\{1,\cdots,L\}$ to one empty slot. The slot with the index α now represents (contains) the firing rate segment $\mathbf{r}([x_s^\alpha, x_e^\alpha])$ (which may, and typically does, consist of multiple spatial bins). In the remaining $N-M$ empty slots, insert the $N-M$ spatial bins of non-field responses (we preserved the order of the non-field bins; this detail is unimportant because non-field responses are of low amplitude and randomizing or not randomizing bin ordering does not lead to quantitatively big effects). The result of this procedure is to exactly preserve the structure of each field, while randomizing the ordering of the fields and also randomizing the gaps (picking new between-field spacings at random, without preserving previous gaps) between fields.

This defines one gap-randomized sample for a given cell. This procedure was used in Figure 5A (reddish-gray), to generate 100 random samples based on the cell in Figure 5A (top). For Figures 5B-5C (reddish-gray), we generated 100 random samples for each cell in our virtual track dataset; this pooled dataset was our full random sample.

To generate gap-shuffled controls, we first note the center-of-mass location of each field (designate the center-of-mass of the αth field by x_c^α; the spatial bin index of this location in the original response is $x_c/\Delta x$), then compute the $L-1$ gaps $g^\alpha \equiv x_c^{\alpha+1} - x_c^\alpha$ between adjacent pairs of the L identified fields (the αth gap length in bins is $g^\alpha/\Delta x$). Next, we randomly permute the indices $\{1,\cdots,L\}$ to get a permuted vector of the indices, $\{c_1,\cdots,c_L\}$ (thus a random ordering of fields), and also randomly permute the indices $\{1,\cdots,L-1\}$ to get another permuted vector $\{d_1,\cdots,d_{L-1}\}$ (thus a random reordering of gaps). We draw at random (uniformly distributed in the interval $[0, N-\sum_{\alpha=1}^{L-1} g^\alpha/\Delta x]$) a location to begin the c_1th field. We assign the gap g^{d_1} next by inserting the corresponding number of empty spatial bins after the first field. At the end of this gap, we place the c_2th field, then gap g^{d_2}, and so on, until all fields and gaps have been assigned. The empty gap bins are now filled in with non-field data, as in the gap-randomized controls above. The result of this procedure is to exactly preserve the structure of each field, and to preserve the set of all gaps from the data in each random control sample; however, a given field is typically adjacent to different gaps than it was in the original data and across different random samples.

As described above, in Figure 5A (bluish-gray) we generated 100 random samples based on the cell in Figure 5A (top). For Figures 5B-5C (bluish-gray), we generated 100 random samples for each cell in our virtual track dataset.

References

Brun V., Solstad T., Kjelstrup K., Fyhn M., Witter M., Moser E., and Moser M.B. (2008). Progressive increase in grid scale from dorsal to ventral medial entorhinal cortex. Hippocampus *18*, 1200–1212.

Domnisoru C., Kinkhabwala A.A., and Tank D.W. (2013). Membrane potential dynamics of grid cells. Nature *495*, 199–204.

Hafting T., Fyhn M., Molden S., Moser M.B., and Moser E. (2005). Microstructure of a spatial map in the entorhinal cortex. Nature *436*, 801–806.

Hill D.N., Mehta S.B., and Kleinfeld D. (2011). Quality metrics to accompany spike sorting of extracellular signals. The Journal of Neuroscience *31*, 8699–8705.

Langston R.F., Ainge J.A., Couey J.J., Canto C.B., Bjerknes T.L., Witter M.P., Moser E.I., and Moser M.B. (2010). Development of the spatial representation system in the rat. Science *328*, 1576–1580.

Yoon K., Buice M.A., Barry C., Hayman R., Burgess N., and Fiete I.R. (2013). Specific evidence of low-dimensional continuous attractor dynamics in grid cells. Nature Neuroscience *16*, 1077–1084.